

Influence of hydration on the thermal transport properties of yttria-doped barium zirconate

Jianqun Gao(高健群), Zhaoyang Wang(王朝阳), Yuhang Jing(荆宇航), and Yufei Gao(高宇飞)
Citation: Chin. Phys. B, 2026, 35 (**2**): 026601. DOI: 10.1088/1674-1056/ae0433
http://cpb.iphy.ac.cn; http://iopscience.iop.org/cpb

What follows is a list of articles you may be interested in

Comparative study of nudged elastic band and molecular dynamics methods for diffusion kinetics in solid-state electrolytes

Aming Lin(林啊鸣), Jing Shi(石晶), Su-Huai Wei(魏苏淮), and Yi-Yang Sun(孙宜阳)
Chin. Phys. B, 2024, 33 (**8**): 086601. DOI: 10.1088/1674-1056/ad5d9a

Hydrogen diffusion in C_1' phase clathrate hydrate

Zixuan Song(宋姿璇), Ziyue Zhou(周子岳), Yanwen Lin(林演文), Qiao Shi(石桥), Yongchao Hao(郝勇超),Yuequn Fu(付越群), Zhisen Zhang(张志森), and Jianyang Wu(吴建洋)
Chin. Phys. B, 2023, 32 (**6**): 066602. DOI: 10.1088/1674-1056/accd4b

Strain effects on Li^+ diffusion in solid electrolyte interphases: A molecular dynamics study

Xiang Ji(姬祥) and Junqian Zhang(张俊乾)
Chin. Phys. B, 2023, 32 (**6**): 066601. DOI: 10.1088/1674-1056/ac9606

Molecular dynamics simulation of thermal conductivity of silicone rubber

Wenxue Xu(徐文雪), Yanyan Wu(吴雁艳), Yuan Zhu(祝渊), Xin-Gang Liang(梁新刚)
Chin. Phys. B, 2020, 29 (**4**): 046601. DOI: 10.1088/1674-1056/ab7743

Tuning the thermal conductivity of strontium titanate through annealing treatments

Liang Zhang(张喨), Ning Li(李宁), Hui-Qiong Wang(王惠琼), Yufeng Zhang(张宇锋), Fei Ren(任飞), Xia-Xia Liao(廖霞霞), Ya-Ping Li(李亚平), Xiao-Dan Wang(王小丹), Zheng Huang(黄政), Yang Dai(戴扬), Hao Yan(鄢浩), Jin-Cheng Zheng(郑金成)
Chin. Phys. B, 2017, 26 (**1**): 016602. DOI: 10.1088/1674-1056/26/1/016602

Influence of hydration on the thermal transport properties of yttria-doped barium zirconate

Jianqun Gao(高健群)[1], Zhaoyang Wang(王朝阳)[2,†], Yuhang Jing(荆宇航)[3], and Yufei Gao(高宇飞)[4]

[1] *School of Electrical and Electronic Engineering, University of Sheffield, Sheffield S*1 3*JD, England*
[2] *School of Intelligent Manufacturing, Nanyang Institute of Technology, Nanyang* 473000, *China*
[3] *Department of Astronautical Science and Mechanics, Harbin Institute of Technology, Harbin* 150001, *China*
[4] *School of Energy and Power Engineering, Dalian University of Technology, Dalian* 116024, *China*

(Received 1 July 2025; revised manuscript received 25 August 2025; accepted manuscript online 8 September 2025)

Perovskites exhibit excellent protonic conductivity in the mid-temperature range, and among them, yttria-doped barium zirconate (BZY) is considered one of the most promising perovskite proton conductors. Molecular simulations provide an efficient approach to investigating the thermal transport behavior of nanocrystalline materials. The effect of doping concentration on the thermal transport properties of BZY structures was investigated using the equilibrium molecular dynamics (EMD) method combined with phonon spectral energy density (SED) analysis. The results show that the thermal transport properties gradually decrease with increasing doping concentration, and for structures with dopants only and without oxygen vacancies, the thermal conductivity exhibits a similar decreasing trend but remains higher than that of structures containing both dopants and oxygen vacancies. Comparison of phonon lifetime and group velocity reveals that oxygen vacancy defects enhance phonon scattering, thereby leading to a reduction in thermal transport properties, while doping reduces the thermal transport properties by weakening lattice harmonicity. The effect of different hydration levels on the thermal transport properties of BZY was also investigated, and the results indicate that the thermal conductivity fluctuates in structures with low hydration levels and continues to decrease as the proton defect concentration increases with hydration. Further analysis of phonon lifetime and group velocity demonstrates that proton defects reduce the thermal transport properties through both enhanced phonon diffusion and weakened harmonicity.

Keywords: molecular dynamics, spectral energy density, hydration, thermal transport property

PACS: 66.70.–f, 02.70.Ns, 63.20.–e, 61.72.S-

DOI: 10.1088/1674-1056/ae0433 **CSTR:** 32038.14.CPB.ae0433

1. Introduction

Perovskite oxides show great potential for proton transport in hydrogen and water vapor environments at 300–800 °C.[1–4] Proton transport occurs through hopping from one ion to the next, making these materials very promising electrolytes for medium-temperature solid oxide fuel cells.[5–9] $BaCeO_3$ (BCO), $SrCeO_3$ (SCO), and $BaZrO_3$ (BZO) perovskites exhibit outstanding potential,[10–17] with BCO and SCO showing poor stability and conductivity at high temperatures,[18] whereas BZO possesses a high melting point and good high-temperature phase stability. However, the high refractoriness, grain-boundary impedance, and poor sintering behavior of BZO result in low conductivity, and yttrium-doped barium zirconate (BZY) successfully overcomes the poor sintering properties and grain-boundary impedance under medium-temperature conditions.[19–21] In addition, BZO is also promising for various other high-temperature applications, such as crucible materials for high-quality crystal growth,[22–25] substrates for thin film deposition,[26,27] and interface materials for ceramic–ceramic composites.[28,29] Therefore, an in-depth study of the thermal transport properties of BZO is needed.

Experimental studies of the thermal conductivity of BZO and BCO show that the thermal conductivity of BZO is approximately three times that of BCO at room temperature and decreases with increasing temperature for both BZO and BCO, indicating dominant phonon-mediated heat transport.[30] Molecular dynamics simulations of the macroscopic thermodynamic properties of BZO revealed that the typical potential wells of Ba–O and Zr–O originate from Coulomb interactions, and the radial distribution function indicates that the atomic structure of $BaZrO_3$ remains dynamically stable at high temperatures. The thermal conductivity was calculated using a nonequilibrium molecular dynamics method, and the simulation results were in good agreement with experimental data.[31] First-principles calculations and experimental studies further revealed that BZO exhibits high phase stability from room temperature to the melting point, good mechanical properties, and low thermal conductivity, while Young's modulus, flexural strength, and thermal conductivity all decrease significantly with increasing temperature.[32] For BZO structures with A- or B-site doping by Ca^{2+}, Sr^{2+}, Ti^{4+}, and Ce^{4+}, experimental studies of microstructure, phase com-

†Corresponding author. E-mail: 15935152219@163.com

© 2026 Chinese Physical Society and IOP Publishing Ltd. All rights, including for text and data mining, AI training, and similar technologies, are reserved.

position, and mechanical and thermal properties showed that $Ba_{1-x}Ca_xZrO_3$ ($x = 0.2$ and 0.4) samples exhibit relatively excellent overall performance. Co-doping with Ca^{2+} and Ti^{4+} at appropriate ratios was further used to enhance the strength and density of the samples, while the thermal conductivity of all doped samples remained generally low.[33] Machine-learning molecular dynamics methods have also been employed to calculate the thermal conductivity and thermal expansion coefficients of BZO and related materials. In these studies, 100 trajectories from *ab initio* molecular dynamics (AIMD) simulations were selected to generate the initial training set, and an active learning approach was used to train the machine-learning potential. The resulting phonon dispersion curves agree well with density functional theory results, thereby validating the accuracy of the machine-learning potential. Based on this potential, homogeneous nonequilibrium molecular dynamics simulations were performed, and the calculated results for materials such as BZO at temperatures up to 1500 K show excellent agreement with experimental measurements.[34]

In this paper, we investigate the thermal transport properties of BZY before and after hydration at different Y-dopant concentrations using Green–Kubo equilibrium molecular dynamics (EMD) simulations and phonon spectral energy density (SED) analysis. By performing EMD simulations for models with different doping concentrations and hydration levels, we demonstrate that oxygen vacancies, dopants, and proton defects all lead to a reduction in the thermal conductivity of BZY. Furthermore, the mechanisms by which hydration reactions affect the thermal transport properties of BZY are elucidated through analysis of phonon correlation properties.

2. Computational theory

2.1. Potential

BZO systems are inorganic ionic compounds, and in this work, the interactions between ions are described using the Coulomb–Buckingham potential function, as expressed in Eq. (1), where q_i and q_j denote the charges of an ionic pair and r_{ij} is the distance between the ions. The first term on the right-hand side represents the short-range repulsive interaction arising from the close proximity of ions. The second term describes the dispersion interaction caused by asymmetry in the electron cloud distribution. This dispersive attraction is weak compared with the Coulomb and repulsive interactions, and because the dispersion coefficient is positive (or zero), the dispersive potential decreases with decreasing interionic distance. The third term represents the Coulomb interaction, which is the most fundamental long-range interaction between ions. The potential parameters A_{ij}, ρ_{ij}, and C_{ij} were empirically derived for each ion–ion interaction. Lattice energy calculations employ the standard Ewald summation method to treat Coulombic interactions, and the ion-pair parameters used in this work are listed in Table 1.[35,36]

$$U = A_{ij}\exp\left(-\frac{r_{ij}}{\rho_{ij}}\right) - \frac{C_{ij}}{r_{ij}^6} + \frac{q_i q_j}{r_{ij}}. \tag{1}$$

Table 1. Potential parameters of Buckingham.

Interaction	A_{ij} (eV)	ρ_{ij} (eV)	$C_{ij}\left(\text{eV}\cdot\text{Å}^6\right)$
$Ba^{2+}\cdots O^{2-}$	931.700	0.3949	0.00
$Zr^{4+}\cdots O^{2-}$	985.869	0.3760	0.00
$Y^{3+}\cdots O^{2-}$	4121.837	0.2804	0.00
$O^{2-}\cdots O^{2-}$	22764.300	0.1490	27.890
$H^{1+}\cdots O^{2-}$	311.97	0.25	0

2.2. EMD simulations

There are two main approaches to modeling atomic-scale heat transport using molecular dynamics simulations. The first approach, known as the EMD method,[37] is based on quantifying heat flow fluctuations in a system at equilibrium at a given temperature, and the Green–Kubo formalism[38] is employed to calculate the thermal conductivity of a bulk material. The second approach, known as the nonequilibrium molecular dynamics (NEMD) method or the direct method,[39] is based on establishing a steady-state heat flow between a heat source and a heat sink and extracting the thermal conductivity of the bulk or the interface from the slope or discontinuity of the temperature gradient, respectively. In this paper, the EMD method is employed to calculate the thermal conductivity of the barium zirconate system.

The calculation of properties such as thermal conductivity using the EMD method is based on fluctuation–dissipation relations and linear response theory. At equilibrium, the heat flow in a particle system fluctuates around zero, and this feature is directly exploited. The heat flow vectors and their time correlations are evaluated throughout the simulation. In this method, the thermal conductivity is related to the heat current autocorrelation function as shown in the following equation:

$$\kappa = \frac{1}{Vk_{\text{B}}T^2}\int_0^{\tau_m}\langle J(\tau)J(0)\rangle\,\mathrm{d}\tau, \tag{2}$$

where V is the volume of the system, k_{B} is the Boltzmann constant, T is the system temperature, τ_m is the correlation time required for sufficient decay of the heat flux autocorrelation function, and $\langle J(\tau)J(0)\rangle$ denotes the ensemble average of the heat flux autocorrelation function.

The heat flow J for systems described by three-body potentials can be calculated using the following equation:

$$\begin{aligned} J(t) =& \sum_i v_i\varepsilon_i + \frac{1}{2}\sum_{ij,i\neq j} r_{ij}\left(F_{ij}\cdot v_i\right) \\ &+\frac{1}{6}\sum_{ijk}\left(r_{ij}+r_{ik}\right)\times\left(F_{ijk}\cdot v_i\right), \end{aligned} \tag{3}$$

where v_i and v_j denote the velocities of atoms i and j, respectively, and F_{ij} is the interatomic force exerted on atom i by

atom j. The first term on the right-hand side represents the convective term, corresponding to heat carried by convective energy transport, while the second and third terms are interaction terms associated with lattice vibrations. Therefore, the EMD method enables decomposition of the contributions to the thermal conductivity from a single simulation result,[40] which is achieved by correlating the integrals for each type of heat flow separately

$$\kappa_{\text{virial}} = \frac{1}{Vk_{\text{B}}T^2}\int_0^{\tau_m} \langle J_{\text{virial}}(\tau)J_{\text{virial}}(0)\rangle \,\mathrm{d}\tau, \tag{4}$$

$$\kappa_{\text{convection}} = \frac{1}{Vk_{\text{B}}T^2}\int_0^{\tau_m} \langle J_{\text{convection}}(\tau)J_{\text{convection}}(0)\rangle \,\mathrm{d}\tau, \tag{5}$$

$$\kappa_{\text{cross}} = \frac{1}{Vk_{\text{B}}T^2}\Big(\int_0^{\tau_m} \langle J_{\text{virial}}(\tau)J_{\text{convection}}(0)\rangle \,\mathrm{d}\tau + \int_0^{\tau_m} \langle J_{\text{convection}}(\tau)J_{\text{virial}}(0)\rangle \,\mathrm{d}\tau\Big), \tag{6}$$

where κ_{virial} is the virial thermal conductivity, representing lattice vibrational heat transfer arising from interatomic potentials; $\kappa_{\text{convection}}$ is the convective thermal conductivity, representing heat transfer due to atomic motion; and κ_{cross} is the cross thermal conductivity, representing the correlation between the virial and convective contributions.

2.3. Calculation of phonon correlation properties

The vibrational density of states (VDOS) is a characteristic quantity that describes the frequency-domain distribution of vibrational modes in a structure and is also referred to as the phonon density of states (PDOS) when describing mode distributions in crystalline materials. It can be obtained using molecular dynamics simulations by performing a Fourier transform of the atomic velocity autocorrelation function[41]

$$\text{VDOS}_\alpha = \frac{1}{N}\sum_i^N \int_{-\infty}^{+\infty} \langle v_{i\alpha}(0)\cdot v_{i\alpha}(t)\rangle \, \mathrm{e}^{-2\pi \mathrm{i}\omega t}, \tag{7}$$

where $v_{i\alpha}$ denotes the velocity component of atom i along the α direction, N denotes the total number of atoms, and ω denotes the angular frequency. The phonon spectral energy density (SED)[42,43] is extracted from the time evolution obtained by molecular dynamics simulations to analyze phonon behavior.[44] The calculation of the phonon spectral energy density is based on mapping the kinetic energy onto phonon normal modes using the phonon eigenvectors

$$\dot{\boldsymbol{q}}\begin{pmatrix}\boldsymbol{k}\\ \lambda\end{pmatrix};t\Big) = \sum_{a,b,n_l}^{3,N_{\text{b}},N}\sqrt{\frac{m_{\text{b}}}{N}}\boldsymbol{v}_\alpha\begin{pmatrix}n_l\\ \lambda\end{pmatrix};t\Big)e^*\begin{pmatrix}\boldsymbol{k} & b\\ \lambda & \alpha\end{pmatrix} \times \exp\left[\mathrm{i}\boldsymbol{k}\cdot r_0\begin{pmatrix}n_l\\ 0\end{pmatrix}\right], \tag{8}$$

where $\boldsymbol{k}$ is the wave vector, λ denotes the phonon mode, α is the Cartesian coordinate direction, N_{b} is the number of atoms in the unit cell, N is the number of unit cells in the system, m denotes the atomic mass, $\boldsymbol{v}$ is the atomic velocity in real space, e^* is the phonon eigenvector, and $\boldsymbol{r}_0$ is the position vector of the unit cell relative to the origin. Based on the normal-mode representation, the phonon spectral energy density can be expressed as

$$\Phi(\boldsymbol{k},\omega) = 2\sum_{\lambda}^{3n}\lim_{\tau_0\to\infty}\frac{1}{2\tau_0}\times\left|\frac{1}{\sqrt{2\pi}}\dot{\boldsymbol{q}}\begin{pmatrix}\boldsymbol{k}\\ \lambda\end{pmatrix}\exp(\mathrm{i}\omega t)\,\mathrm{d}t\right|, \tag{9}$$

where ω is the angular frequency of the phonon mode and t denotes time. After obtaining the spectral energy density, the phonon lifetime can be extracted by fitting the half-width of the spectral peak using a Lorentzian function

$$\Phi(\boldsymbol{k},\omega) = \frac{I}{1+[(\omega-\omega_{\text{c}})/\gamma]^2}, \tag{10}$$

$$\tau = \frac{1}{2\gamma}, \tag{11}$$

where I denotes the peak intensity, γ denotes the half-width at half-maximum of the peak, ω_{c} denotes the peak angular frequency, and τ denotes the phonon lifetime.

3. Results and discussion

The EMD method has been widely used to investigate the thermal conductivity of perovskite materials and has produced reliable results using both $8\times8\times8$ and $10\times10\times10$ supercell models.[31,40] EMD simulations employing $5\times5\times5$, $6\times6\times6$, $8\times8\times8$, $10\times10\times10$, and $12\times12\times12$ BZO supercells indicate that the calculated thermal conductivity is insensitive to the supercell size. In this work, a $10\times10\times10$ supercell was selected to facilitate construction of structures with different doping concentrations. Based on the BZO structure, different concentrations of Y^{3+} were used to randomly substitute Zr^{4+}, and a corresponding number of lattice oxygen atoms were removed to form oxygen vacancies in order to maintain charge neutrality, yielding Y-doped BZY structures. On this basis, oxygen vacancies were filled with different concentrations of OH^-, and H^+ ions were introduced near neighboring lattice oxygen atoms to obtain hydrated BZY structures. The atomic structures of BZO, Y-doped BZY, and fully hydrated BZY are shown in Fig. 1. In the simulations, periodic boundary conditions were applied in all three directions, and the initial structures were first energy-minimized using the conjugate gradient method. The initial atomic velocities were assigned according to the Boltzmann distribution at 300 K, and a time step of 0.5 fs was used. The systems were first equilibrated at 300 K for 100 ps using the NPT ensemble, followed by further equilibration at 300 K for 100 ps using the NVT ensemble to ensure thermal equilibrium. Subsequently, production runs of 2000 ps were carried out in the NVE ensemble, during which the heat flux was recorded to compute the heat flux

autocorrelation function and the thermal conductivity according to Eqs. (2)–(6). The equations of motion were integrated using the velocity Verlet algorithm. To ensure statistical reliability, different initial atomic velocities were generated using different random seeds, and the reported thermal conductivities represent averages over 20 independent simulations for each structure.

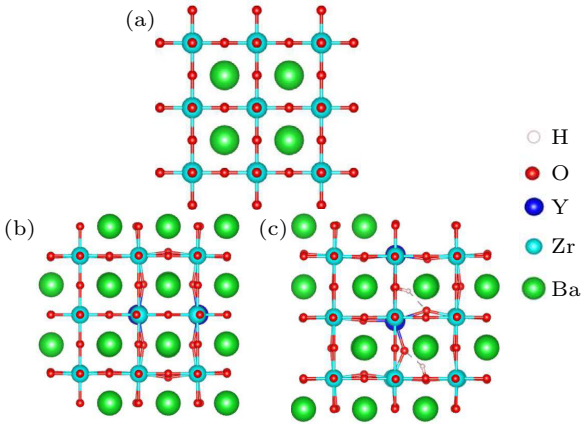


Fig. 1. Atomic configurations of BZO (a), BZY (b), and hydrated BZY (c).

3.1. Influence of doping concentration on the thermal transport properties of BZY

To investigate the effect of doping concentration on the thermal transport properties, additional structures with Y doping concentrations of 2%, 5%, 10%, 15%, 20%, 25%, and 30%, together with the corresponding fully hydrated structures, were constructed. The total number of atoms in each structure, as well as the numbers of Y^{3+} ions, oxygen vacancies ($V_O^{\cdot\cdot}$), and H^+ defects, are summarized in Table 2. The thermal conductivity of these structures was calculated using the EMD method with a simulation setup consistent with that used for calculating the thermal conductivity of BZO in Section 3.

For different doping concentrations and the corresponding fully hydrated structures, the variations of the total thermal conductivity, virial thermal conductivity, convective thermal conductivity, and coupling thermal conductivity are shown in Fig. 2. In the EMD method, the virial thermal conductivity reflects the contribution from lattice vibrations driven by potential energy interactions, while the convective thermal conductivity corresponds to energy transport arising from fluid-like atomic motion. From a mathematical perspective, the cross-correlation function between the convective and virial heat fluxes is negative, which leads to a negative cross thermal conductivity. This indicates that the fluctuations of the two components tend to cancel each other: when the convective heat flux increases, the virial heat flux tends to decrease, resulting in a partial offset of energy transport. Under this mechanism, convection does not simply enhance heat conduction but instead acts to weaken the overall thermal conductivity.

Table 2. Ionic numbers of systems.

System	Total number of atoms	Y^{3+} number	$V_O^{\cdot\cdot}$ number	H^+ number
BZO	5000	0	0	0
BZY2	4990	20	10	0
BZY5	4975	50	25	0
BZY10	4950	100	50	0
BZY15	4925	150	75	0
BZY20	4900	200	100	0
BZY25	4875	250	125	0
BZY30	4850	300	150	0
Fully hydrated BZY2	5020	20	0	20
Fully hydrated BZY5	5050	50	0	50
Fully hydrated BZY10	5100	100	0	100
Fully hydrated BZY15	5150	150	0	150
Fully hydrated BZY20	5200	200	0	200
Fully hydrated BZY25	5250	250	0	250
Fully hydrated BZY30	5300	300	0	300

From a broader perspective, convection can be understood as a complex extension of conduction,[45] where solid lattice vibrations and fluid-like atomic motion are described within a unified mathematical framework. In this framework, the energy flux is closely related to the velocity component $v\cos\theta$ (where θ denotes the angle between the convective velocity and the direction of energy propagation). Since this component can take negative values, negative contributions to thermal conductivity may arise under certain conditions, highlighting the role of velocity orientation in energy transport. It is worth emphasizing that although the cross term is negative, the total thermal conductivity always remains positive, because the positive contributions from the virial and convective parts far outweigh the offset from the cross term. Moreover, with increasing yttrium doping concentration, lattice distortion becomes more pronounced and ion motion is further restricted, thereby weakening the negative coupling between convection and vibration.

The fluid-like motion of Ba^{2+} ions in the structure gives rise to a significant convective thermal conductivity, and Y doping weakens this convective contribution, which gradually decreases with increasing Y doping concentration. The convective contribution associated with Ba^{2+} ion motion is negatively coupled with the vibrational heat transport of the Zr–O framework, leading to a strong suppression effect and resulting in a total thermal conductivity lower than the virial thermal conductivity. The thermal conductivity of the undoped and defective BZO structure is 16.41 W/mK, which is larger than the experimentally reported value of 5.75 W/mK,[24] and this discrepancy arises because the simulation employs a perfect crystalline structure, whereas experimentally prepared samples inevitably contain defects generated during the sintering process. According to previous reports,[46] the thermal conductivity of 20% La^{3+}-doped barium zirconate at room temperature is 2.8 W/mK, while our simulation yields a value of

2.75 W/mK for 20% Y^{3+}-doped barium zirconate. These values are in very close agreement, and considering that La and Y induce similar structural distortions due to their comparable ionic radii, this consistency strongly supports the reliability and accuracy of the present simulations.

When the BZO structure is doped with Y ions and oxygen vacancies are introduced, the thermal conductivity of the system decreases significantly. With increasing doping concentration and oxygen vacancy concentration, the thermal conductivity of the BZY structure continues to decrease, although the rate of decrease gradually slows down. When the doping concentration reaches 30%, the thermal conductivity is reduced to 1.99 W/mK, corresponding to a decrease of about 88%. This behavior is consistent with experimental observations that B-site cation doping leads to a substantial reduction in the thermal conductivity of BZO. For the corresponding fully hydrated BZY structures, the variation of thermal conductivity is shown in Fig. 2(b). Upon complete hydration, oxygen vacancy defects are occupied by hydroxide ions (OH-) to form proton defects, and the number of proton defects is twice that of the oxygen vacancy defects, as summarized in Table 2. The increased defect concentration further reduces the thermal conductivity. For the BZY structure with a doping concentration of 30%, the thermal conductivity decreases to 1.86 W/mK after hydration, corresponding to an additional reduction of about 6.5% compared to the dehydrated case, and an overall decrease of 88.7% relative to the perfect BZO structure.

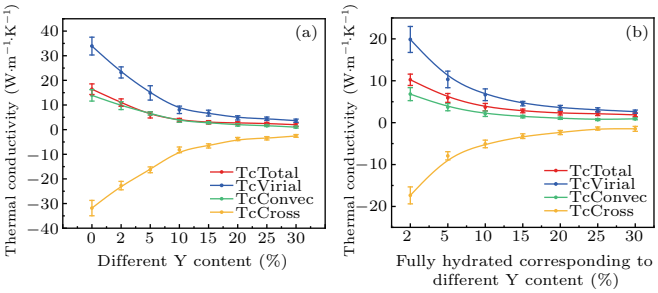


Fig. 2. Thermal conductivity of BZY (a) and fully hydrated BZY (b) with different doping concentrations.

During the doping process, two types of defects, namely impurities and oxygen vacancies, are introduced into the BZO crystal simultaneously. To investigate the effect of doping on the thermal transport properties, the thermal conductivity of the Y-doped structure without oxygen vacancies (denoted as BZYO) was additionally calculated. The model was constructed based on the doped structures listed in Table 2, where the number and positions of the Y ions were kept the same as in the corresponding models, while all oxygen vacancies were filled with O ions. The calculated thermal conductivity results are shown in Fig. 3. Compared with the thermal conductivity of the doped structures containing oxygen vacancy defects shown in Fig. 2(a), the lattice vibrations in the doped structures without oxygen vacancies yield a higher virial thermal conductivity, leading to a higher total thermal conductivity than that of the structures containing oxygen vacancy defects. At a low doping concentration of 2%, the decrease in thermal conductivity is small. As the doping concentration increases, the thermal conductivity exhibits a pronounced decrease and then gradually approaches saturation. This decreasing trend is consistent with that observed in the doped structures containing oxygen vacancies. When the doping concentration reaches 30%, the thermal conductivity of the structure without oxygen vacancies is 5.56 W/mK, corresponding to a reduction of about 66.1% compared with the pristine BZO structure.

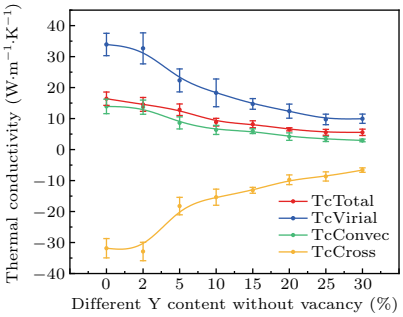


Fig. 3. Thermal conductivity of different doping concentrations BZY without oxygen vacancies.

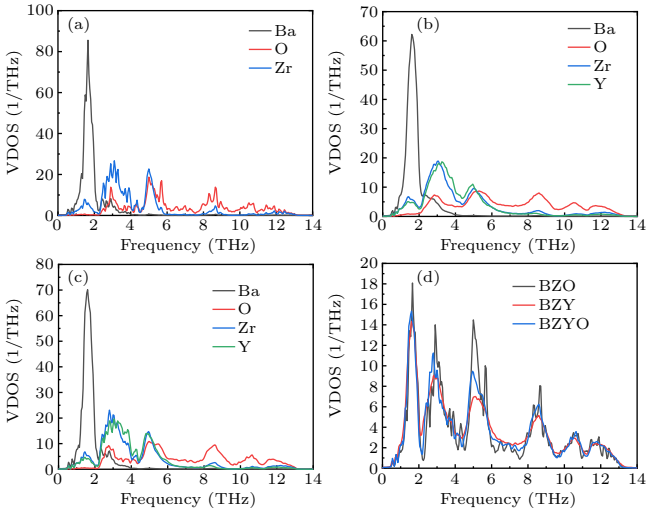


Fig. 4. Vibrational density of state for different atoms in BZO (a), BZY (b), and BZYO (c), and structure (d).

To understand the mechanism by which changes in atomic motion affect the thermal conductivity, the VDOS of different atomic species in BZO, BZY20 (denoted as BZY), and BZY20 without oxygen vacancy defects (denoted as BZYO) were calculated by performing a Fourier transform of the atomic velocity autocorrelation functions. The corresponding results are shown in Fig. 4. As shown in Figs. 4(a)–4(c), the VDOS of the Ba–O lattice is mainly concentrated in the low-frequency range of 0–2 THz, whereas the VDOS of the Zr–O lattice is primarily distributed over three frequency regions, namely 2–4 THz, 4.6–6 THz, and 8–9 THz. The VDOS

distribution range of the Y–O lattice is similar to that of the Zr–O lattice. The total vibrational density of states of the different structures is shown in Fig. 4(d). Compared with the pristine BZO structure, the doped structures exhibit a reduced VDOS peak intensity accompanied by a slight elevation of the trough regions, indicating that doping enhances the non-monochromaticity of lattice vibrations, which in turn leads to a reduction in thermal conductivity.

To further investigate the mechanism of thermal conductivity reduction induced by doping and oxygen vacancy defects from a phonon perspective, the phonon lifetimes of BZO, BZY20, and BZY20 without oxygen vacancy defects were calculated using the SED method. The phonon dispersion relations were obtained by solving the dynamical matrix, and the phonon group velocity was calculated according to $\boldsymbol{v}_{\mathrm{g}} = \partial\boldsymbol{\omega}/\partial\boldsymbol{q}$, where $\boldsymbol{\omega}$ and $\boldsymbol{q}$ denote the phonon eigenfrequencies and wavevectors, respectively. The calculated phonon lifetimes and phonon group velocities are shown in Fig. 5. As shown in Fig. 5(a), there is little difference between the phonon lifetimes of the BZYO and BZO structures, whereas the phonon lifetime of the BZY structure is significantly reduced in the frequency range of 0–20 THz. This result indicates that Y doping alone has a relatively minor effect on phonon scattering, while the oxygen vacancies introduced during the doping process substantially enhance phonon scattering, thereby increasing the thermal resistance and reducing the thermal transport capability of the structure. As shown in Fig. 5(b), the phonon group velocities of the BZY and BZYO structures are markedly reduced in the frequency range of 0–25 THz compared with that of the BZO structure, whereas the difference between the BZY and BZYO structures is relatively small. This indicates that Y doping suppresses phonon group velocity by weakening lattice harmonicity, thereby degrading the thermal transport performance.

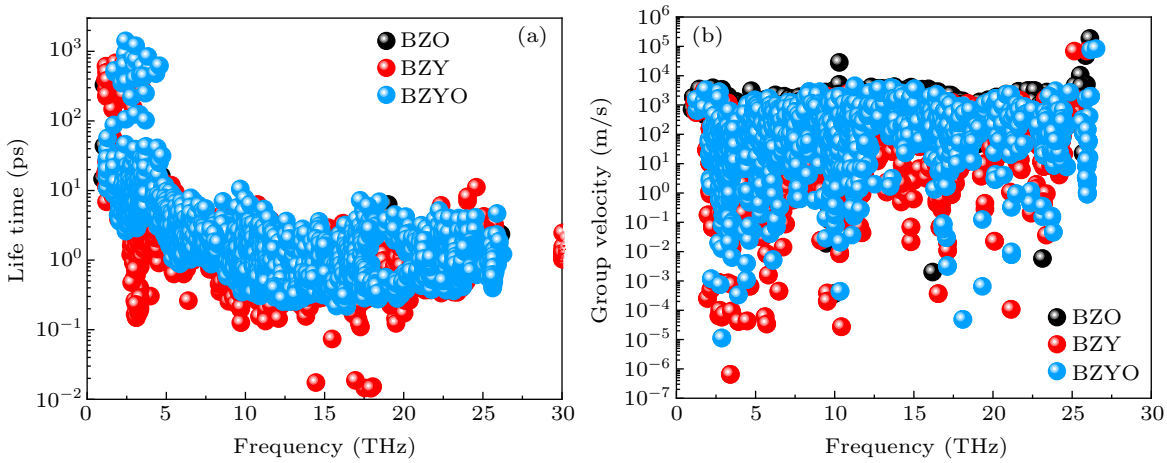


Fig. 5. Comparison of phonon lifetime (a) and phonon group velocity (b).

To investigate the effect of the hydration reaction on the thermal transport properties, BZY structures with hydration levels of 2%, 5%, 10%, 20%, 40%, 60%, and 80% were additionally constructed for the BZY system with a fixed Y doping concentration of 20%. Table 3 summarizes the total number of atoms for each structure, as well as the corresponding numbers of Y^{3+} ions, oxygen vacancies, and H^{+} ions. The thermal conductivity of these structures was calculated using the EMD method, with a simulation setup consistent with that used for the BZO thermal conductivity calculation in Section 3.

For structures with different hydration levels, the variation in thermal conductivity is shown in Fig. 6. At low hydration levels ($< 20\%$), the contributions from the virial and convective terms exhibit no pronounced changes, whereas the cross term shows noticeable fluctuations. This behavior arises because the cross term is evaluated from the autocorrelation between kinetic-energy and potential-energy heat currents, whose magnitudes differ significantly, leading to numerical fluctuations in the calculated thermal conductivity. For the unhydrated structure with 20% Y doping, the thermal conductivity is 2.75 W/mK. When hydration begins, oxygen vacancies are gradually occupied by hydroxide ions, and the thermal conductivity exhibits fluctuations. Once the hydration level exceeds 20%, the thermal conductivity decreases monotonically. Upon complete hydration, the thermal conductivity is reduced to 2.26 W/mK, corresponding to a decrease of approximately 17.8% relative to the unhydrated structure.

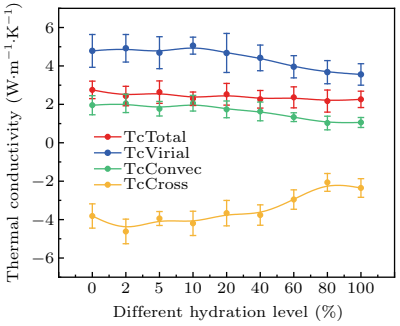


Fig. 6. Thermal conductivity of BZY with different hydration levels.

The vibrational density of states of different atomic species in the fully hydrated BZY structure and the corresponding unhydrated BZY structure with 20% Y doping were calculated by Fourier transforming the atomic velocity autocorrelation functions, and the results are shown in Fig. 7. As shown in Fig. 7(a), the VDOS distributions of the Ba–O, Zr–O, and Y–O lattices are consistent with those of the BZY structure shown in Fig. 4(b), whereas the VDOS of H ions is mainly distributed in the frequency ranges of 12.6–16.5 THz and 18.3–21.9 THz. As shown in Fig. 7(b), the presence of H ions exerts a passivating effect on lattice vibrations, suppressing phonon modes in the low-frequency range of 0–12.5 THz. This suppression further weakens the thermal transport properties of the hydrated structure.

Table 3. Ionic numbers of systems.

System	Total number of atoms	Y^{3+} number	$V_0^{\cdot\cdot}$ number	H^+ number
BZY20	4900	200	100	0
2% hydrated BZY20	4906	200	98	4
5% hydrated BZY20	4915	200	95	10
10% hydrated BZY20	4930	200	90	20
20% hydrated BZY20	4960	200	80	40
40% hydrated BZY20	5020	200	60	80
60% hydrated BZY20	5080	200	40	120
80% hydrated BZY20	5140	200	20	160
Fully hydrated BZY20	5200	200	0	200

To investigate the mechanism by which hydration reduces thermal conductivity through phonon properties, the phonon lifetimes and group velocities of the fully hydrated BZY20 structure (hydrated BZY, Fig. 8) were calculated using the same method described previously. The results are shown in Fig. 8.

As shown in Fig. 8(a), the phonon lifetimes of the hydrated BZY structure are significantly reduced compared to those of the pristine BZO structure. The introduction of proton defects during the hydration reaction further decreases the phonon lifetimes across the frequency range of 0–25 THz, indicating that these defects substantially enhance phonon scattering, which leads to a reduction in thermal transport properties.

From Fig. 8(b), it can be seen that hydration also suppresses the phonon group velocities of the structure in the same frequency range, weakening lattice harmonicity and thereby decreasing thermal transport performance. These results demonstrate that proton defects introduced during hydration reduce the thermal conductivity of BZY through both enhanced phonon scattering and weakened harmonicity.

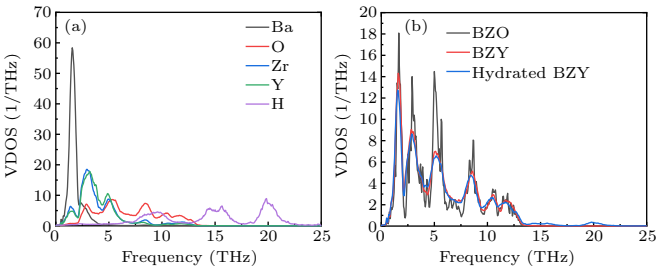


Fig. 7. Vibrational density of states of different atoms in fully hydrated BZY (a) and structure (b).

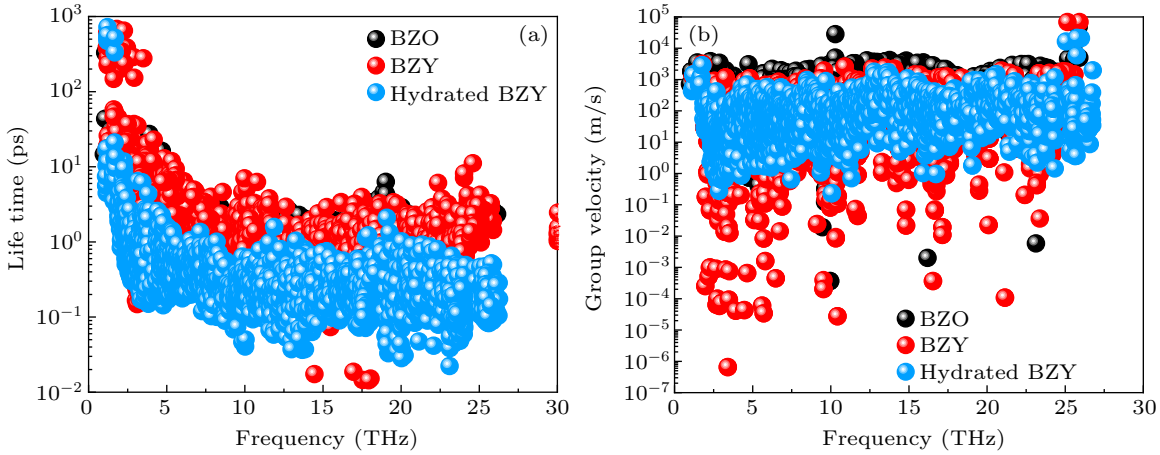


Fig. 8. Comparison of phonon lifetime (a) and phonon group velocity (b).

4. Conclusion

In this work, we investigated the effect of hydration on the thermal transport properties of BZY using the Coulomb-Buckingham potential in EMD simulations combined with phonon correlation analysis.

The results show that the thermal conductivity of BZY gradually decreases with increasing Y doping concentration and the presence of oxygen vacancy defects. Hydration further reduces the thermal transport properties by introducing proton defects. For structures with only Y doping but without oxygen vacancies, the thermal conductivity also decreases, but remains higher than that of structures containing both dopants and oxygen vacancies.

Analysis of phonon lifetimes and phonon group velocities

indicates that oxygen vacancy defects enhance phonon scattering, while Y doping suppresses lattice harmonicity, both of which contribute to the reduction in thermal transport performance. For BZY with 20% Y doping, different hydration levels were considered: at low hydration levels, the thermal conductivity exhibits slight fluctuations, whereas higher hydration levels lead to a continuous decrease due to the increasing concentration of proton defects. Overall, hydration reduces the thermal transport performance by approximately 17.8% relative to the unhydrated structure. Phonon analysis confirms that proton defects simultaneously enhance phonon scattering and weaken harmonicity, resulting in decreased thermal conductivity from both effects.

This study provides an in-depth characterization of thermal transport in yttria-doped barium zirconate, offering insights that are instructive for the further design and application of perovskite electrolyte materials.

Acknowledgments

Project supported by the National Natural Science Foundation of China (Grant No. 12172112) and the National Natural Science Foundation of China (Joint Fund for Corporate Innovation and Development – Key Program) (Grant No. U22B2082).

References

[1] Fabbri E, Pergolesi D and Traversa E 2010 *Chem. Soc. Rev.* **39** 4355
[2] Liu Y, Fu M, Zhang Y, Liu J, Liu K and Tao Z 2024 *J. Electroanal. Chem.* **961** 118204
[3] Loganathan S, Biswas S, Kaur G and Giddey S 2024 *Processes* **12** 2278
[4] Kindelmann M, Escolastico S, Almar L, Vayyala A, Jennings D, Deibert W, Meulenberg W, Rheinheimer W, Bram M, Serra J, Mayer J and Guillon O 2024 *J. Mater. Chem. A* **12** 3977
[5] Duan C, Huang J, Sullivan N and O'Hayre R 2020 *Appl. Phys. Rev.* **7** 011314
[6] Meng Y, Gao J, Zhao Z, Amoroso J, Tong J and Brinkman K S 2019 *J. Mater. Sci.* **54** 9291
[7] Hou J, Miao L, Hui J, Bi L, Liu W and Irvine J T 2018 *J. Mater. Chem. A* **6** 10411
[8] Rehman J, Hanif M B, Khan M Z, Ullah M, Starostina I A, Muhammad M T and Li Z 2024 *Energy Fuels* **38** 22637
[9] Mikami Y, Sekitani Y, Yamauchi K, Kuroha T and Okuyama Y 2024 *ACS Appl. Energy Mater.* **7** 1136
[10] Chen G, Gao P, Kang J, Li B, Ali W, Qin Z, Lu X and Li C 2017 *J. Alloys Compd.* **726** 403
[11] Løken A, Saeed S W, Getz M N, Liu X and Bjørheim T S 2016 *J. Mater. Chem. A* **4** 9229
[12] Lindman A, Helgee E E and Wahnström G 2017 *Chem. Mater.* **29** 7931
[13] Wang B, Bi L and Zhao X S 2018 *J. Power Sources* **399** 207
[14] Anjaneya K C, Nayaka G P, Manjanna J, Kumar V A, Govindaraj G and Ganesha K N 2014 *J. Alloys Compd.* **598** 33
[15] Yadav D, Nirala G, Yadav S, Kumar U, Upadhyay S and Kumar S 2021 *Appl. Phys. A* **127** 964
[16] Radenahmad N, Afroze S, Afif A, Azad A T, Shin J S, Park J Y, Zaini J H and Azad A K 2020 *Ionics* **26** 1297
[17] Sammes N, Phillips R and Smirnova A 2004 *J. Power Sources* **134** 153
[18] Medvedev D A, Lyagaeva J G, Gorbova E V, Demin A K and Tsiakaras P 2016 *Prog. Mater. Sci.* **75** 38
[19] Bi L, Daás E H and Shafi S P 2017 *Electrochem. Commun.* **80** 20
[20] Chen G, Luo Y, Sun W, Liu H, Ding Y, Li Y, Geng S, Yu K and Liu G 2018 *Int. J. Hydrog. Energy* **43** 12765
[21] Zając W, Rusinek D, Zheng K and Molenda J 2013 *Open Chem.* **11** 471
[22] Alford N M, Templeton A and Penn S J 1998 *Supercond. Sci. Technol.* **11** 703
[23] Kamitani A, Wakana H, Adachi S and Tanabe K 2004 *Phys. C Supercond.* **412** 1414
[24] He D, Feng Q, Fu Y, Zhang M, Chen G, Gao P and Li C 2024 *J. Mater. Res. Technol.* **33** 9726
[25] Shen Y, Hong D, Sun T, Hou R, Zheng G, Niu Y and Chen G 2025 *J. Asian Ceram. Soc.* **13** 89
[26] Dierickx D, Houben I, Lapin J, Delannay F and Van Der Biest O 1996 *J. Mater. Sci. Lett.* **15** 1573
[27] Grammatika N, McLachlan D S and Sonnenberg N 1993 *Supercond. Sci. Technol.* **6** 469
[28] Koopman M, Duncan S, Chawla K K and Coffin C 2001 *Compos. Part Appl. Sci. Manuf.* **32** 1039
[29] Chen Z C, Tamachi T, Kulkarni R, Chawla K K and Koopman M 2008 *J. Eur. Ceram. Soc.* **28** 1149
[30] Yamanaka S, Hamaguchi T, Oyama T, Matsuda T, Kobayashi S and Kurosaki K 2003 *J. Alloys Compd.* **359** 1
[31] Goh W F, Khan S A and Yoon T L 2013 *Model. Simul. Mater. Sci. Eng.* **21** 045001
[32] Liu Y, Zhang W, Wang B, Sun L, Li F, Xue Z, Zhou G, Liu B and Nian H 2018 *Ceram. Int.* **44** 16475
[33] Qiao Z, Li S, Li Y, Xu N and Xiang K 2022 *Ceram. Int.* **48** 12529
[34] Zeraati M, Oganov A R, Fan T and Solodovnikov S F 2024 *Phys. Rev. Mater.* **8** 033601
[35] Stokes S J and Islam M S 2010 *J. Mater. Chem.* **20** 6258
[36] Raiteri P, Gale J D and Bussi G 2011 *J. Phys. Condens. Matter* **23** 334213
[37] Volz S G and Chen G 2000 *Phys. Rev. B* **61** 2651
[38] Schelling P K, Phillpot S R and Keblinski P 2002 *Phys. Rev. B* **65** 144306
[39] Schelling P K and Phillpot S R 2001 *J. Am. Ceram. Soc.* **84** 2997
[40] Gao Y, Ning W, Zhang X, Liu Y, Zhou Y and Tang D 2021 *Nano Energy* **82** 105747
[41] Bao H, Chen J, Gu X and Cao B 2018 *ES Energy Environ.* **1** 16
[42] Wang Z, Feng T and Ruan X 2015 *J. Appl. Phys.* **117** 084317
[43] Zhang X, Bao H and Hu M 2015 *Nanoscale* **7** 6014
[44] Wang F, Sun Y, Zou Y, Xu B and Fu B 2023 *Chin. Phys. B* **32** 096301
[45] Xu L and Huang J 2020 *Chin. Phys. Lett.* **37** 080502
[46] Li Y, Qiao Z, Li S, Liu F and Tan J 2024 *Ceram. Int.* **50** 18750